A Parameterization Scheme Accounting for Nonhydrostatic Effects on the Momentum Flux of Vertically Propagating Orographic Gravity Waves: Formulas and Preliminary Tests in the Model for Prediction Across Scales (MPAS)

XIN XU,[a,b,c] RONGRONG ZHANG,[a,b] MIGUEL A. C. TEIXEIRA,[d] ANNELIZE VAN NIEKERK,[e] MING XUE,[f] YIXIONG LU,[g] HAILE XUE,[g] RUNQIU LI,[a,b] AND YUAN WANG[a,b]

[a] *Key Laboratory of Mesoscale Severe Weather, Ministry of Education, Nanjing University, Nanjing, Jiangsu, China*
[b] *School of Atmospheric Sciences, Nanjing University, Nanjing, Jiangsu, China*
[c] *CMA Radar Meteorology Key Laboratory, Nanjing, Jiangsu, China*
[d] *Department of Meteorology, University of Reading, Reading, United Kingdom*
[e] *European Centre for Medium-Range Weather Forecasts, Reading, United Kingdom*
[f] *Center for Analysis and Prediction of Storms, University of Oklahoma, Norman, Oklahoma*
[g] *CMA Earth System Modeling and Prediction Centre, Beijing, China*

(Manuscript received 16 February 2023, in final form 5 February 2024, accepted 6 February 2024)

ABSTRACT: The momentum transport by orographic gravity waves (OGWs) plays an important role in driving the large-scale circulation throughout the atmosphere and is subject to parameterization in numerical models. Current parameterization schemes, which were originally developed for coarse-resolution models, commonly assume that unresolved OGWs are hydrostatic. With the increase in the horizontal resolution of *state-of-the-art* numerical models, unresolved OGWs are of smaller horizontal scale and more influenced by nonhydrostatic effects (NHE), thus challenging use of the hydrostatic assumption. Based on the analytical formulas for nonhydrostatic OGWs derived in our recent study, the orographic gravity wave drag (OGWD) parameterization scheme in the Model for Prediction Across Scales is revised by accounting for NHE. Global simulations with 30-km horizontal resolution are conducted to investigate NHE on the momentum transport of OGWs and their impacts on the large-scale circulation in boreal winter. NHE are evident in regions of complex terrain such as the Tibetan Plateau, Rocky Mountains, southern Andes, and eastern Antarctica. The parameterized surface wave momentum flux can be either reduced or enhanced depending on the relative importance of NHE and model physics–dynamics interactions. The NHE corrections to the OGWD scheme significantly reduce the easterly biases in the polar stratosphere of the Northern Hemisphere, due to both weakened OGWD in the upper troposphere and lower stratosphere and suppressed upward propagation of resolved waves into the stratosphere. However, the revised OGWD scheme only has a weak influence on the large-scale circulation in the Southern Hemisphere during boreal winter.

KEYWORDS: Gravity waves; Mountain waves; Stratospheric circulation; Nonhydrostatic models; Parameterization

1. Introduction

It is well recognized that internal gravity waves excited by flow over topography play a significant role in the momentum and energy budgets of large-scale circulations throughout the atmosphere (e.g., Fritts and Alexander 2003; Alexander et al. 2010; Sandu et al. 2019). Orographically forced gravity waves (OGWs) are thus considered to be an important process that mediates the coupling between the troposphere and middle atmosphere.

In general, OGWs have a broad range of wavelengths ranging from a few to hundreds of kilometers. A large portion of these OGWs cannot be resolved in coarse-resolution numerical weather prediction (NWP) and general circulation models (GCMs). Recent studies showed that even high-resolution (9 km) global NWP models do not resolve OGWs sufficiently (Kruse et al. 2022; Polichtchouk et al. 2023). Various parameterization schemes have been developed to take into account the impact of subgrid-scale OGWs on the mean flow, which is often known as orographic gravity wave drag (OGWD) (Palmer et al. 1986; McFarlane 1987; Kim and Arakawa 1995; Lott and Miller 1997; Scinocca and McFarlane 2000; Webster et al. 2003; Kim and Doyle 2005; Choi and Hong 2015). The implementation of OGWD parameterization schemes has proven efficient in reducing the systematic biases seen in GCMs. For example, it can help separate the stratospheric polar night jet from the tropospheric subtropical jet and alleviate the delayed breakdown of the Southern Hemisphere polar vortex by reducing the too strong stratospheric winds (e.g., Alexander et al. 2010; McLandress et al. 2012; Garcia et al. 2017; Lu et al. 2020). Parameterizing subgrid-scale OGWD can also help improve the simulation of the East Asian monsoon circulation and precipitation (Choi et al. 2017; Zhang et al. 2020; Li et al. 2023) and contribute to the reduction of wet biases over the western Tibetan Plateau in winter (Zhou et al. 2017) in weather forecast and regional models.

Nevertheless, unresolved OGWs and their interaction with the large-scale circulation remain a large source of uncertainties in climate modeling (Shepherd 2014; Eichinger et al. 2020; Šácha et al. 2021). This is attributed not only to the inaccurate theoretical treatment of the momentum transport by OGWs in parameterization schemes, but also to the lack of observational constraints on parameterized OGWD (Sandu et al. 2019). For

Corresponding author: Xin Xu, xinxu@nju.edu.cn

DOI: 10.1175/JAS-D-23-0020.1

example, current parameterization schemes only account for the drag effect of OGWs, that is, a force that roughly opposes the mean flow. However, as noted by Shutts (1995), the OGWs generated in directionally sheared flows can produce a force perpendicular to the mean flow, i.e., orographic gravity wave lift (Xu et al. 2019; van Niekerk et al. 2023). The directional absorption of OGWs can inhibit wave breaking in the troposphere by reducing the wave amplitude and transporting more wave momentum flux (WMF) upward into the stratosphere and mesosphere (Xu et al. 2018, 2019). In this work, of particular interest is the hydrostatic assumption that has been employed by OGWD parameterization schemes since the 1980s when numerical models had very coarse resolution on the order of $O(100)$ km. At these coarse resolutions, the dominant scale of the subgrid-scale orography (SSO) is broad enough so that nonhydrostatic effects (NHE), which act to decrease the WMF through horizontal dispersion of wave energy (Klemp and Durran 1983; Xue and Thorpe 1991; Zängl 2003), may be omitted. However, global NWP models have experienced rapid development in the last ten years, with *state-of-the-art* models reaching resolutions $O(1)$ km, e.g., the Integrated Forecasting System (IFS) of the European Centre for Medium-range Weather Forecasts (ECMWF) (Polichtchouk et al. 2023). Consequently, the largest horizontal scales of the unresolved orography have decreased, such that more of the subgrid-scale OGWs are affected by NHE. This is not to say that NHE do not affect the OGWD in coarser resolution models. But at finer horizontal resolutions NHE are likely to have a much bigger impact on the subgrid-scale waves (because nonhydrostatic OGWs are expected to carry a significant portion of the momentum fluxes). These waves will be erroneously represented if parameterized as hydrostatic or entirely neglected. Although OGWD parameterizations become less important with the increase of model resolution as a larger part of the OGWs spectrum is resolved, high-resolution simulations (e.g., Kruse et al. 2022) have suggested that the OGWD parameterizations remain important even with rather high resolutions. In this regard, OGWD parameterization schemes that incorporate NHE are required to keep pace with the development of high-resolution NWP and climate models.

Recently, Xu et al. (2021, hereafter X21) theoretically studied the impact of NHE on the surface WMF of vertically propagating OGWs excited by idealized three-dimensional (3D) elliptical terrain, which is a key component in OGWD parameterization schemes. An analytical expression was derived for the surface WMF using Taylor expansions formally valid for weakly nonhydrostatic conditions, introduced in Teixeira et al. (2008) for nonhydrostatic OGWs forced by two-dimensional (2D) ridges. In this approach, the degree of nonhydrostaticity is measured by a nondimensional parameter called "horizontal Froude number," i.e., $\mathrm{Fr} = \sqrt{U^2 + (\gamma V)^2}/NL_x$ where (U, V) is the base-state horizontal wind velocity, N is the Brunt–Väisälä frequency, and $\gamma = L_x/L_y$ is the orography anisotropy with L_x and L_y being the half-widths of orography in the x and y directions, respectively. The horizontal Froude number is akin to the traditional Froude number $\mathrm{Fr} = \sqrt{U^2 + V^2}/Nh_0$ that is often used to quantify the nonlinearity of OGWs (e.g., Miranda and James 1992), with the mountain height (h_0) replaced by its width (L) in the denominator. Physically, the horizontal Froude number quantifies the ratio between the period of buoyancy oscillations and the advection time of flow past the mountain. For slow airflow and/or broad orography (i.e., $\mathrm{Fr} \to 0$), the OGWs are predominantly hydrostatic. As Fr increases, NHE become more and more important.

The asymptotic solution expressing the surface WMF in X21 was formally derived for weakly nonhydrostatic OGWs. Fortunately, it was shown to be in a very good agreement with the exact solution obtained by numerical integration, even at large Fr, i.e., for highly nonhydrostatic OGWs. Thus, this analytical solution can be adopted to revise the surface WMF (i.e., wave source) in the OGWD parameterization schemes by accounting for NHE, which (as explained above) are increasingly important in high-resolution NWP and climate models. This approach provides a physically based, flow-dependent, alternative to simply filtering out the WMF associated with OGWs shorter than a prescribed scale, e.g., 5 km, as in existing OGWD schemes. As mentioned above, there are a variety of OGWD parameterization schemes. Herein, we choose the scheme developed by Kim and Doyle (2005, hereafter KD05), which has been implemented in the Weather Research and Forecast (WRF) Model (Skamarock et al. 2008) as well as the Model for Prediction Across Scales (MPAS) (Skamarock et al. 2012). The performance of the revised scheme that accounts for NHE is then evaluated using online simulations of the MPAS model. It is also possible to revise other OGWD schemes, such as the Lott and Miller (1997, hereafter LM97) scheme adopted in the IFS model of ECMWF and Unified Model (UM) of the Met Office among other models (van Niekerk et al. 2020) using the same approach.

The rest of this paper is organized as follows. Section 2 first introduces the asymptotic expressions for NHE on the surface WMF as derived in X21 and their implementation in the revised KD05 parameterization scheme. The setup of global simulations using the MPAS model is then described. Section 3 investigates the influence of NHE on the parameterized WMF and OGWD and their impacts on the large-scale circulation. Finally, the paper is summarized and discussed in section 4.

2. Data and methods

a. *Theoretical formulas for NHE*

For nonhydrostatic OGWs generated by airflow over 3D elliptical bell-shaped mountains, asymptotic expressions were derived in X21 for NHE on the surface WMF along the x and y directions of a given Cartesian frame of reference, respectively:

$$\mathrm{NHE}_x = \frac{\tau_{x\_\mathrm{nonhydrostatic}}}{\tau_{x\_\mathrm{hydrostatic}}} - 1 = -I_2(\mathrm{Fr}) - \frac{1}{2}\mathrm{Fr}^2 I_4(\mathrm{Fr}) R_x(\gamma, \psi), \tag{1}$$

$$\mathrm{NHE}_y = \frac{\tau_{y\_\mathrm{nonhydrostatic}}}{\tau_{y\_\mathrm{hydrostatic}}} - 1 = -I_2(\mathrm{Fr}) - \frac{1}{2}\mathrm{Fr}^2 I_4(\mathrm{Fr}) R_y(\gamma, \psi), \tag{2}$$

where τ_x and τ_y are the WMFs in the x and y directions, respectively; ψ is the direction of the horizontal wind (defined as zero along x); and

$$I_2(\mathrm{Fr}) = (2\mathrm{Fr}^{-2} + 2\mathrm{Fr}^{-1} + 1)e^{-2\mathrm{Fr}^{-1}}, \tag{3}$$

$$I_4(\mathrm{Fr}) = 3 - (2\mathrm{Fr}^{-4} + 4\mathrm{Fr}^{-3} + 6\mathrm{Fr}^{-2} + 6\mathrm{Fr}^{-1} + 3)e^{-2\mathrm{Fr}^{-1}}, \tag{4}$$

$$R_x(\gamma, \psi_H) = \frac{\int_0^{\pi} \frac{\cos\phi \cos^3(\phi - \psi)}{\sqrt{\cos^2\phi + \gamma^2 \sin^2\phi}} d\phi}{\int_0^{\pi} \frac{\cos\phi \cos(\phi - \psi)}{\sqrt{\cos^2\phi + \gamma^2 \sin^2\phi}} d\phi}, \tag{5}$$

$$R_y(\gamma, \psi_H) = \frac{\int_0^{\pi} \frac{\sin\phi \cos^3(\phi - \psi)}{\sqrt{\cos^2\phi + \gamma^2 \sin^2\phi}} d\phi}{\int_0^{\pi} \frac{\sin\phi \cos(\phi - \psi)}{\sqrt{\cos^2\phi + \gamma^2 \sin^2\phi}} d\phi}, \tag{6}$$

where ϕ is the azimuth of the horizontal wave vector. Equations (1) and (2) give the fraction of surface WMF corrected by NHE. These corrections are always negative, indicating a decrease of surface WMF due to lateral wave energy dispersion. NHE depend not only on Fr but also on the terrain anisotropy and the horizontal wind direction. Calculation of the integrals in Eqs. (5) and (6) has a considerable computational cost when the complete expressions are used in practice. Fortunately, the two factors R_x and R_y, which are related to the terrain anisotropy and the horizontal wind direction, have a very weak influence on NHE, especially at low Fr less than 1 (see Figs. 5 and 7 in X21). In the case of circular orography (i.e., $\gamma = 1$), the isotropic NHE have a simple form, depending on Fr only:

$$\mathrm{NHE}_c(\mathrm{Fr}) = -\frac{9}{8}\mathrm{Fr}^2 + e^{-2\mathrm{Fr}^{-1}}\left(-\frac{5}{4}\mathrm{Fr}^{-2} - \frac{1}{2}\mathrm{Fr}^{-1} + \frac{5}{4} + \frac{9}{4}\mathrm{Fr} + \frac{9}{8}\mathrm{Fr}^2\right), \tag{7}$$

where the subscript c indicates circular orography. Figure 1 displays the variation of NHE with the horizontal Froude number. The magnitude of the NHE shows an increasing trend with the horizontal Froude number, reaching up to 35% at Fr = 0.5. The expression in Eq. (7) involves algebraic manipulations only. Thus, it can be readily used to modify the surface WMF in OGWD parameterization schemes (e.g., the KD05 scheme), which were originally developed for hydrostatic OGWs.

b. *Revision of the KD05 scheme*

The surface WMF of vertically propagating OGWs, which is called reference-level WMF in the KD05 scheme, is given by

$$\tau_0 = \rho_0 E \frac{m}{\lambda_{\mathrm{eff}}} G \frac{|\mathbf{V}_L|^3}{N_L}, \tag{8}$$

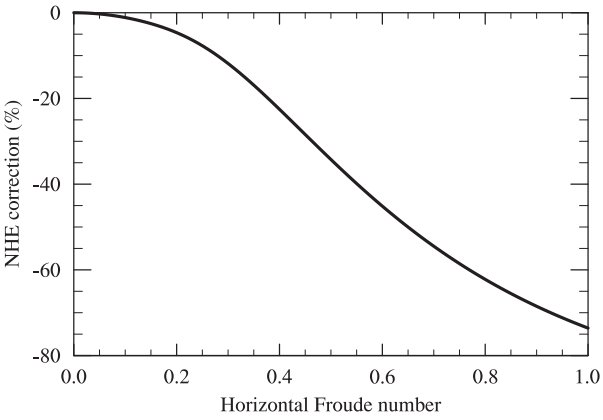

FIG. 1. Variation of the NHE correction with the horizontal Froude number.

where

$$E = (\mathrm{OA} + 2)^{C_E \mathrm{Fr}_0/\mathrm{Fr}_c}, \quad m = (1 + L_x)^{\mathrm{OA}+1},$$
$$G = \frac{\mathrm{Fr}_0^2}{\mathrm{Fr}_0^2 + C_G \mathrm{OC}^{-1}}, \quad \mathrm{Fr}_0 = \frac{2\sigma_h N_L}{|\mathbf{V}_L|}\mathrm{OD}. \tag{9}$$

In the above equations, the factor E represents the effect of stress enhancement due to low-level wave breaking and/or lee wave trapping, which is influenced by the shape and location of the SSO within the model grid cell and the flow nonlinearity measured by the traditional Froude number Fr_0. The factor G provides a smooth transition between blocking and nonblocking flow regimes that is determined using the criterion of whether or not the traditional Froude number exceeds the critical value $\mathrm{Fr}_c = 1$. The factor m is the "number of mountains" within the grid cell, which estimates the bulk volume of the SSO, and λ_{eff} is the effective grid length used as a tunable coefficient. The variables ρ_0, $|\mathbf{V}_L|$, and N_L are the air density, horizontal wind speed, and buoyancy frequency averaged in a lower layer between surface and $2\sigma_h$ above the surface, with σ_h being the standard deviation of the SSO height. The KD05 scheme takes into account the orographic asymmetry (OA), orographic convexity (OC) (i.e., sharpness and slope), and orographic direction (OD) of the SSO, where $\mathrm{OD} = L_x^{\perp}/L_x$ is the SSO anisotropy with L_x and $L_x^{\perp}$ being the effective orographic lengths along and perpendicular to the low-level mean wind $\mathbf{V}_L$, respectively. Finally, the two constants $C_E = 0.8$ and $C_G = 0.5$ are empirically calibrated using the mesoscale numerical simulations of Kim and Arakawa (1995).

To account for NHE, the reference-level WMF given by Eq. (8) is revised according to Eq. (7), that is,

$$\tilde{\tau}_0 = \tau_0[1 + \mathrm{NHE}_c(\mathrm{Fr})], \tag{10}$$

with the horizontal Froude number calculated from the low-level mean horizontal wind, buoyancy frequency and the SSO length in the along-flow direction. Note that the NHE corrections are not applied to the flow-blocking stress because the flow blocking dynamics are essentially different from that of OGWs.

Above the reference level, the WMF is propagated gradually upward until reaching the model top. At each model level, the flow stability is checked by examining the wave-modulated Richardson number:

$$\widetilde{\mathrm{Ri}}_m = \frac{\overline{\mathrm{Ri}}(1 - \mathrm{Fr}_d)}{(1 + \overline{\mathrm{Ri}}^{1/2}\mathrm{Fr}_d)^2}, \tag{11}$$

where $\overline{\mathrm{Ri}} = \overline{\mathrm{Ri}}(z)$ is the mean-flow Richardson number, and $\mathrm{Fr}_d = h_d(z)N(z)/|\mathbf{V}(z)|$ with h_d being the wave amplitude. [Here $\mathbf{V}(z)$ is the horizontal wind projected onto the direction of low-level mean flow, i.e., $\mathbf{V}_L$.] Wave breaking and momentum deposition are activated once the wave-modulated Richardson number drops below a critical value of 0.25 (Lindzen 1981). The wave amplitude is determined by

$$(h_d^2)_i = \frac{\Delta x}{m}\frac{\tau_{i+1}}{\rho_i N_i |\mathbf{V}(z)|_i}, \tag{12}$$

where Δx is the horizontal grid size, and the subscript i denotes the model-level index decreasing upward. Readers are referred to KD05 for more details about the parameterization scheme.

c. Setup of numerical simulations

In this work, we use the atmospheric component of the MPAS v7.0 model, i.e., MPAS-A. The dynamical core of the MPAS-A model solves the fully compressible nonhydrostatic equations of motion, which are cast in terms of a geometric-height vertical coordinate, along with numerical schemes similar to that employed in the Advanced Research WRF model. The physics suite of the MAPS-A model is also taken from the Advanced Research WRF model, including the OGWD parameterization. Readers are referred to Skamarock et al. (2012) for more details about the dynamics and physics of the MAPS-A model.

Two sets of global simulations are conducted using, respectively, the original KD05 scheme (i.e., EXP_KD05) and the revised scheme taking into account NHE on the vertically propagating waves as derived in X21 (i.e., EXP_X21). Both experiments consist of 35 individual runs from 0000 UTC 25 November to the end of December in each year of the period 1980–2014, with 6-h output interval. The model initial conditions are obtained from the ERA-Interim reanalysis (i.e., ERA-I), with a spatial resolution of 0.75° × 0.75° (Dee et al. 2011). The first 5 days of simulations are considered as the model spinup time. The 1-month outputs in December are averaged to obtain the 35-yr average. The MPAS-A model is configured with a horizontal resolution of 30 km, given the computational cost of the global simulations. In the vertical there are 41 levels, with the model top placed at approximately 10 hPa. An integration time step of 180 s is used. The default "mesoscale reference" suite is adopted for the model physics, which includes the WRF single-moment 6-class (WSM6) microphysics scheme, the RRTMG longwave and shortwave radiation scheme, the Yonsei University (YSU) planetary boundary layer (PBL) scheme, the Monin–Obukhov surface layer scheme, the Noah land surface model, and the new Tiedtke scheme for parameterization of cumulus convection.

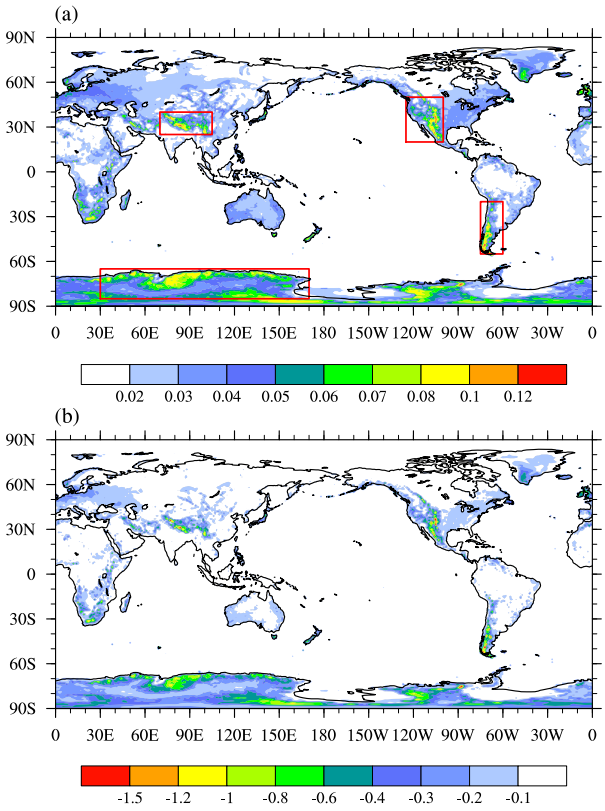

FIG. 2. Geographical distributions of (a) horizontal Froude number and (b) NHE correction (units: %) averaged over December 1980–2014 in EXP_X21. The red rectangles in (a) represent the regions of the Tibetan Plateau, Rocky Mountains, southern Andes, and eastern Antarctica, respectively.

3. Results

a. Distribution of horizontal Fr and NHE corrections

Figure 2 presents the geographical distributions of the horizontal Froude number and NHE corrections averaged in December of 1980–2014 in experiment EXP_X21. It is worth noting that the NHE corrections given in Fig. 2b are calculated online according to Eq. (7), which is always negative. However, the differences between the parameterized WMFs in the two experiments can be either negative or positive (see section 3b), given the interaction and feedback between the model dynamics and physics. That is, the changes in the parameterized OGWD modify the flow resolved by the model (wind speed, stability, etc.), which in turn affects the parameterization of subgrid-scale OGWD. As shown in Fig. 2a, the OGWs in the regions of highly complex terrain, e.g., the Tibetan Plateau, Rocky Mountains, southern Andes, and eastern Antarctica, are most prone to be affected by NHE, where the horizontal Froude number can exceed 0.1, associated with the most relevant NHE corrections (Fig. 2b).

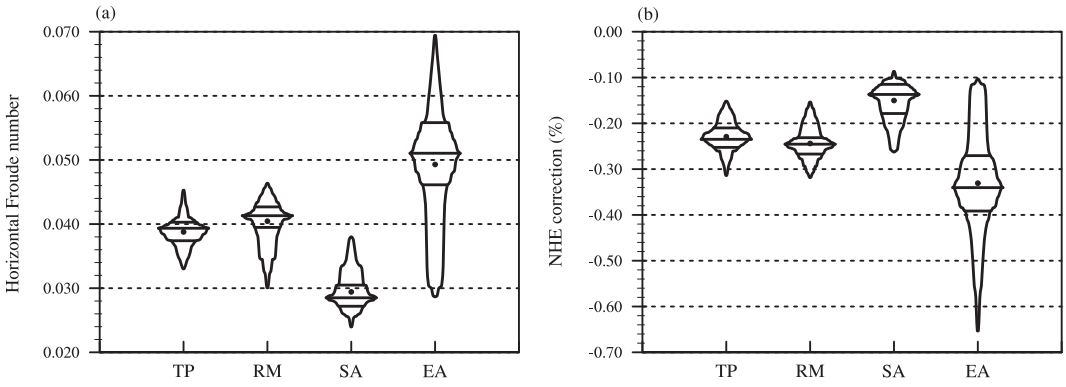

FIG. 3. Statistical distributions of the (a) horizontal Froude number and (b) NHE correction (units: %) averaged in the four hotspot regions of the Tibetan Plateau (TP), Rocky Mountains (RM), southern Andes (SA), and eastern Antarctica (EA).

Figure 3a displays the statistical distributions of the areal-mean horizontal Froude number in the four hotspot regions mentioned above to reveal their intermittency. (The domain average is only made for grids with SSO higher than 10 m.) The mean horizontal Froude number is about 0.04 in both the regions of the Tibetan Plateau and Rocky Mountains. However, the horizontal Froude number over the Rocky Mountains exhibits a wider distribution (i.e., more intermittent) than the former. The horizontal Froude number over the southern Andes is in general smaller than in the former two regions, showing a smaller mean value of about 0.03. By contrast, the horizontal Froude number over eastern Antarctica is on average larger than in the other three hotspot regions, with a mean value up to about 0.05. It is also characterized by the largest intermittency, which varies between 0.03 and 0.07. Figure 3b is similar to Fig. 3a but for the NHE corrections in Fig. 2b. Therefore, the intermittency of the NHE directly matches that of the horizontal Froude number.

b. *Impacts on the WMF and OGWD*

Figure 4a gives the vertical distribution of the zonal-mean absolute WMF of parameterized OGWs in EXP_KD05. The zonal-mean WMF has a larger magnitude in the mid- to high latitudes of the Northern Hemisphere where the major mountainous ranges (e.g., the Tibetan Plateau and Rocky Mountains) are present. This is consistent with the results of WRF simulations in Xu et al. (2019) (see their Fig. 5a). Notable WMF values are also found in the polar regions of the Southern Hemisphere. By contrast, the WMF is relatively weak in the lower latitudes and tropics, which are mostly covered by oceans. In particular, parameterized WMF is totally absent around the latitudinal band of 60°S, i.e., over the Southern Ocean. This is due to the fact that the KD05 scheme makes use of the single-column assumption, which cannot account for the lateral propagation of OGWs from nearby orography, e.g., the southern Andes and the Antarctic Peninsula (Hasha et al. 2008; Song and Chun 2008; Jiang et al. 2014; Ehard et al. 2017). As height increases, the WMF is reduced owing to wave breaking. The WMF in the mid- to high latitudes of both hemispheres (except around 60°S) can be transported upward into the stratosphere, especially in the Northern Hemisphere around 45°N, which appears to be an atmospheric window for OGWs (Xu et al. 2019). On the contrary, the WMF in the lower latitudes and tropics is predominantly attenuated in the troposphere, with little leakage into the stratosphere. As will be shown in the next subsection, this is due to the presence of a zonal wind reversal between the lower-tropospheric easterlies and upper-tropospheric westerlies in the tropics, which forms a critical level that prevents OGWs from propagating upward into the stratosphere.

Figure 4c depicts the differences between the zonal-mean WMF magnitudes in EXP_KD05 and EXP_X21 (i.e., EXP_X21 minus EPX_KD05). Notable differences are mainly located in the middle and high latitudes. In the region of 30°–50°N, the parameterized WMF in EXP_X21 tends to be smaller than in EXP_KD05 below about 400 hPa, due to the NHE corrections. As height increases, the parameterized WMF is enhanced in the upper troposphere and lower stratosphere below about 70 hPa, while it weakens again higher up. Similarly, the parameterized WMF south of about 75°S is first reduced in the lower troposphere below about 700 hPa and then enhanced in the middle and upper troposphere, followed by weakening in the stratosphere. This will be interpreted below as a redistribution of WMF in the vertical. In contrast, there is enhancement of lower-tropospheric WMF at the latitudes of about 70°, 50°S and north of 60°N. This is, as mentioned earlier, ascribed to the interaction and feedback between the parameterized OGWD and the resolved flow. According to Eq. (8), the surface WMF of OGWs increases with the low-level wind speed. The decrease of surface WMF by NHE can first lead to a reduction of low-level OGWD (via suppression of wave breaking) and hence increase of low-level wind, which in turn enhances the surface WMF. Therefore, the changes of WMF are dependent on the relative importance of NHE and model physics–dynamics interaction and feedback. The latter appears to dominate locally in these latitudes. In addition, the changes of WMF with height are different in these regions. The WMF is always enhanced near 70°S, 50°S and 60°N. Yet, in the high latitudes north of about 65°N, weakening of WMF dominates in the mid- to upper troposphere and stratosphere.

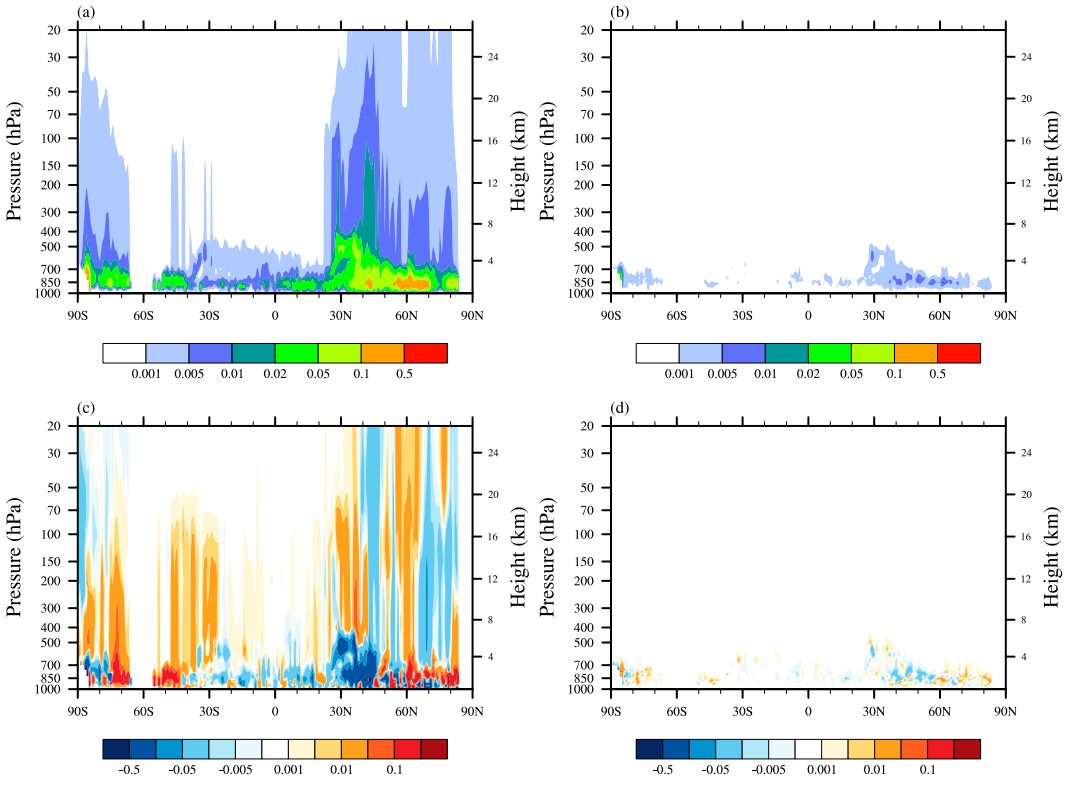

FIG. 4. Vertical distribution of (a) the magnitude of zonal-mean WMF of OGWs (units: kg m^{-1} s^{-2}) in EXP_KD05, and (c) the difference (exaggerated by 100 times for clarity) between the magnitudes of zonal-mean WMF of OGWs (units: kg m^{-1} s^{-2}) in EXP_X21 and EXP_KD05 (EXP_X21 minus EXP_KD05) averaged over December 1980–2014. (b),(d) As in (a) and (c), but for the flow blocking stress.

Moreover, the KD05 scheme also includes the parameterization of low-level flow blocking. Figures 4b and 4d are similar to Figs. 4a and 4c but for the flow blocking stress. It is evident that the flow blocking stress is mainly located in the lower troposphere and is about one order smaller than the WMF of OGWs. Although the NHE corrections are not applied to the flow blocking stress, as noted in section 2b, this stress also changes when accounting for NHE in EXP_X21. This is due to the variation of the model-resolved flow. Nonetheless, the changes of flow blocking stress are much weaker than those of the WMF.

The above analyses show that the NHE corrections can affect the upward transport of WMF. As OGWD is caused by the vertical divergence of the WMF, it will be affected by the changes in the upward transport of the WMF. Figure 5a presents the vertical distribution of the zonal-mean OGWD magnitude in EXP_KD05 averaged over December 1980–2014. The differences between the OGWD in EXP_KD05 and EXP_X21 (i.e., EXP_X21 minus EXP_KD05) are given in Fig. 5c. In the midlatitudes of the Northern Hemisphere, there is notable OGWD in the lower troposphere, upper troposphere and lower stratosphere (Fig. 5a), i.e., below and above the tropospheric jet, in agreement with the WRF simulations of Xu et al. (2019). The upper-level OGWD is favored by the decrease of air density with altitude and the relatively weak horizontal winds existing between the tropospheric jet and polar night jet, i.e., the so-called "valve layer" (Kruse et al. 2016). Remarkable OGWD is also found in the lower troposphere of the polar regions of the Southern Hemisphere.

Compared to that in EXP_KD05, the OGWD in EXP_X21 is basically reduced in the lower troposphere of the Northern Hemisphere's midlatitudes (30°–50°N) and the Southern Hemisphere's polar region (south of about 75°S). This is due to the decrease of lower-tropospheric WMF by the NHE corrections (Fig. 4c), which reduces the wave amplitude [according to Eq. (12)] and thus suppresses wave breaking. As a result, more WMF is transported upward to the upper troposphere and lower stratosphere (Fig. 4c), leading to greater wave breaking and stronger OGWD there (Fig. 5c). Given the additional deposition of wave momentum at lower levels, the WMF that can be transported upward to the mid- to upper stratosphere is decreased (Fig. 4c), which in turn causes a weakening of OGWD (Fig. 5c). This vertical structure of "weakened–enhanced–weakened" OGWD is similar to that in Xu et al. (2020, 2019). In these two studies, the changes of OGWD are caused by the impact of vertical wind shear and curvature on the surface WMF and the selective critical-level absorption by directional wind shear, respectively. Other processes such as lateral wave propagation and other wave sources can also cause vertical redistribution of the WMF and

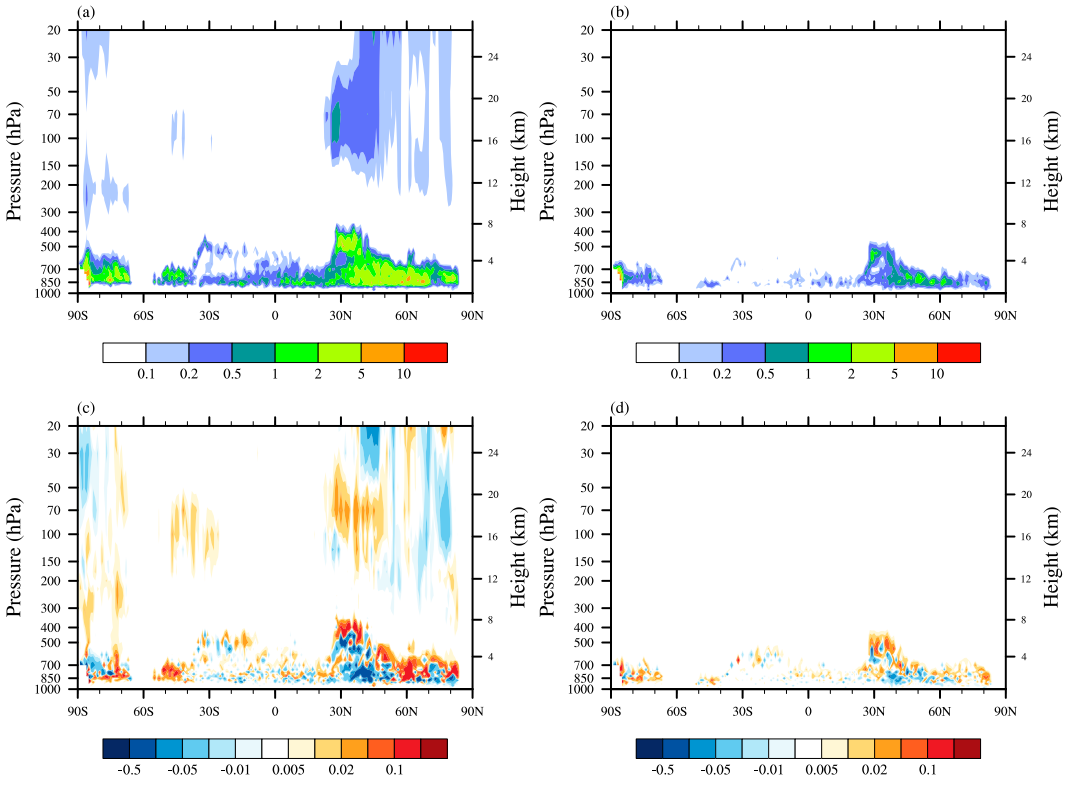

FIG. 5. Vertical distributions of (a) zonal-mean OGWD magnitude (units: m s^{-1} day^{-1}) in EXP_KD05, and (c) the difference between the magnitudes of zonal-mean OGWD (units: m s^{-1} day^{-1}) in EXP_X21 and EXP_KD05 (EXP_X21 minus EXP_KD05) averaged over December 1980–2014. (b),(d) As in (a) and (c), but for the FBD.

OGWD (e.g., Sato et al. 2012; de la Cámara et al. 2016; Xu et al. 2017b).

In the high latitudes north of about 65°N, the OGWD is mainly enhanced in the troposphere but reduced in the stratosphere (Fig. 5c). This is because the enhancement of surface WMF (Fig. 4c) causes greater wave breaking and more wave momentum deposition in the troposphere, which reduces the amount of WMF that can be transported upward to the stratosphere. Near the latitudes of 70° and 50°S where the surface WMF is also enhanced, however, the OGWD increases in both the troposphere and stratosphere. This means that the increased wave momentum deposition in the lower troposphere is totally compensated for by the enhancement of surface WMF. As such, there is still more WMF transported upward to the upper troposphere and stratosphere (Fig. 4c), leading to stronger OGWD there. Figures 5b and 5d are similar to Figs. 5a and 5c but for the flow blocking drag (FBD). Consistent with the behavior of the flow blocking stress (Fig. 4c), the FBD is mainly located in the lower troposphere (Fig. 5b). The most evident FBD occurs in the Northern Hemisphere's midlatitudes as well as Antarctica, but the FBD is obviously weaker than the OGWD. The changes of FBD are also much weaker than their OGWD counterparts (Fig. 5d).

Figure 6 additionally shows the statistical distributions of the OGWD in the upper troposphere and lower stratosphere (i.e., 200–20 hPa) of the Northern Hemisphere's high latitudes (i.e., 60°–90°N) in the two experiments. Compared to those in EXP_KD05, both the upper and lower limits of the OGWD (especially the latter) are reduced in EXP_X21. Therefore, the mean OGWD becomes systematically weakened after the NHE corrections.

The different responses of OGWD to the NHE corrections reflect the complexity of OGWD parameterization which relies on both the wave source and the mean flow conditions that support the propagation of OGWs. The NHE corrections applied to the wave source, albeit weak, can affect the upward transport of WMF and thus the OGWD. In the next section, the impacts of the revised OGWD scheme on the simulated large-scale circulation will be studied.

c. *Impacts on the large-scale circulation*

Figures 7a and 7b compare the vertical distributions of the zonal-mean zonal wind averaged over December 1980–2014, obtained from ERA-I and EXP_KD05, respectively, with their difference (EXP_KD05 minus ERA-I) given in Fig. 7c. In boreal winter, the midlatitudes of the Northern Hemisphere are dominated by westerlies in both the troposphere and stratosphere, with a tropospheric jet located at about 200 hPa (Fig. 7a). A stratospheric westerly jet is found in the high latitudes, which is the lower part of the polar night jet, separated from the tropospheric jet. There also exists a subtropical jet in the troposphere

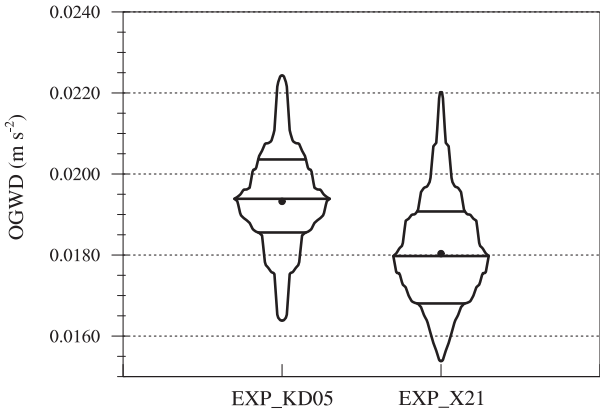

FIG. 6. Statistical distribution of the OGWD in the upper troposphere and lower stratosphere (i.e., 200–20 hPa) of the Northern Hemisphere's high latitudes (i.e., 60°–90°N).

of the Southern Hemisphere, which is much weaker than its Northern Hemisphere counterpart. In contrast, easterlies are found to prevail in the stratosphere of the Southern Hemisphere. The experiment EXP_KD05 in general reproduces the structure of the zonal-mean zonal wind, such as the tropospheric jet and stratospheric jet (Fig. 7b). Yet, there are still discrepancies between the MPAS simulation and ERA-I. Notable easterly wind biases are found in the upper troposphere and stratosphere north of 50°N, which can exceed -12 m s^{-1} (Fig. 7c). Relatively weak easterly biases are found in the mid- to upper troposphere between about 20°S and 40°N and in the stratosphere around 30°S. In contrast, there are westerly wind biases in the stratosphere of the Northern Hemisphere's mid- to low latitudes (0°–40°N) and the Southern Hemisphere's high latitudes (south of 50°S), which are weaker than the aforementioned easterly wind biases.

Figure 7d is similar to Fig. 7c but shows the differences between the zonal-mean zonal winds in EXP_KD05 and EXP_X21 (i.e., EXP_KD05 minus EXP_X21). In the tropics and lower latitudes, there are few differences between the zonal-mean zonal winds, owing to the negligible NHE occurring there (Fig. 2). The largest wind differences occur in the mid- to high latitudes of the Northern Hemisphere (north of about 50°N) where the zonal-mean zonal winds are increased by more than 2 m s^{-1} in the stratosphere. In contrast, there is a decrease of zonal-mean zonal winds (by less than 1 m s^{-1}) in the troposphere, which slightly degrades the simulation. Most of these wind differences are statistically significant at the 95% confidence level according to the Student's *t* test. As shown in Fig. 5c, the OGWD generally weakens in the polar stratosphere of the Northern Hemisphere, despite some enhancement around 60°N. The weakening of the stratospheric OGWD favors the strengthening of westerly winds. Moreover, as found in previous studies, the zonal winds in the polar stratosphere of the Northern Hemisphere can also be affected

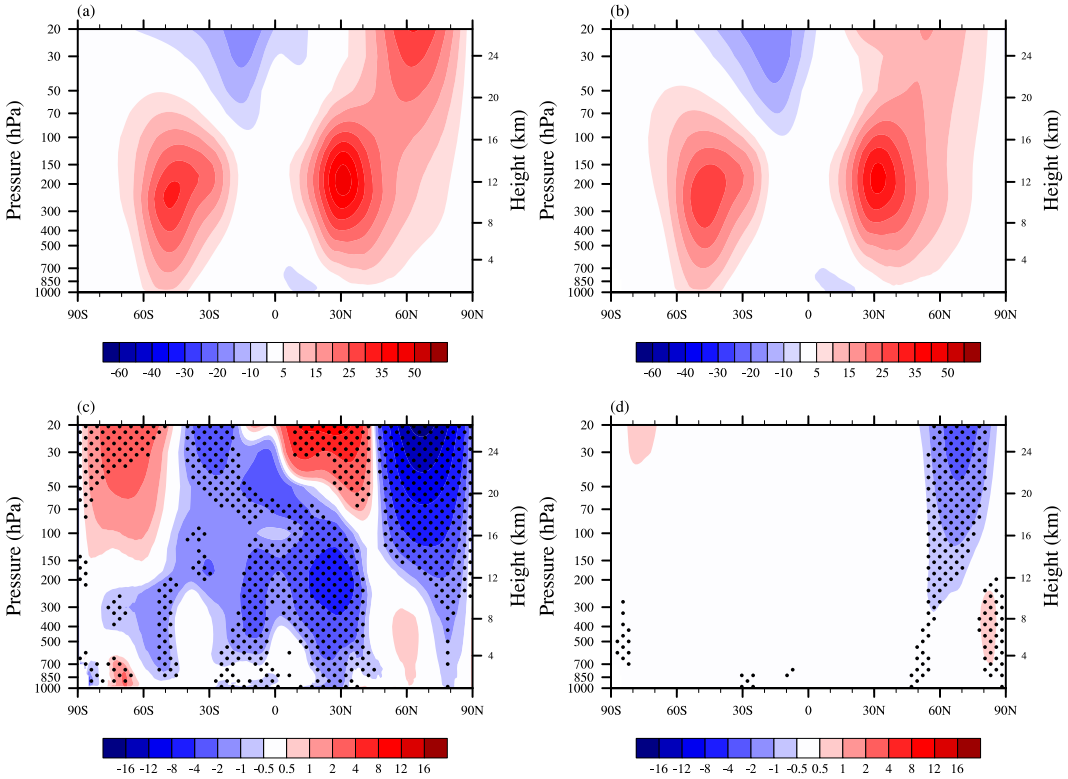

FIG. 7. Vertical distributions of zonal-mean zonal wind (units: m s^{-1}) averaged over December 1980–2014 obtained from (a) ERA-I and (b) EXP_KD05, with (c) their difference (EXP_KD05 minus ERA-I). (d) As in (c), but for the difference between EXP_KD05 and EXP_X21 (EXP_KD05 minus EXP_X21). Stippling denotes differences that are statistically significant at the 95% confidence level.

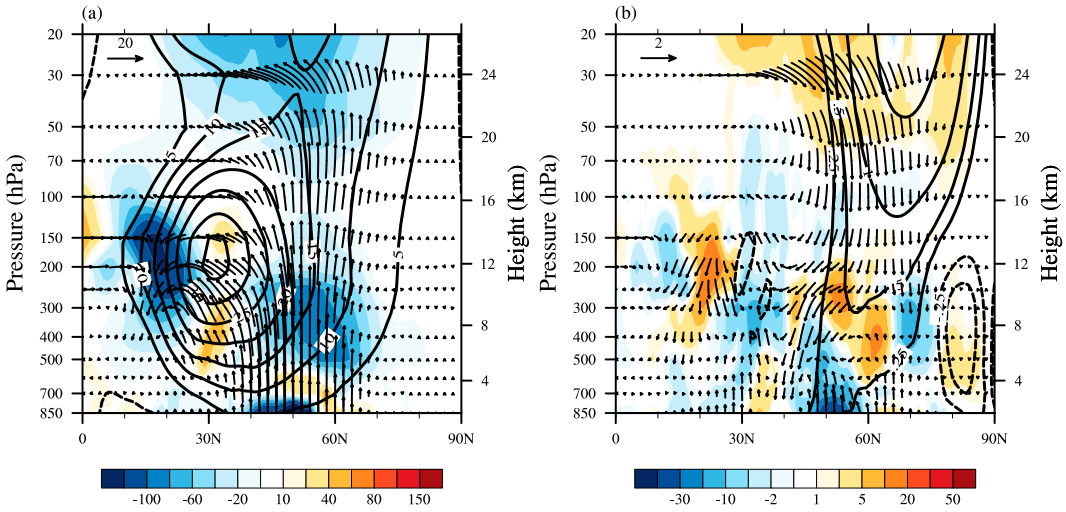

FIG. 8. (a) Zonal-mean EP flux (arrows) and its divergence (shading; units: $m^2\ s^{-2}$) in EXP_KD05 averaged over December 1980–2014. Contours are the zonal-mean zonal winds (units: $m\ s^{-1}$). (b) As in (a), but for the differences between EXP_X21 and EXP_KD05 (EXP_X21 minus EXP_KD05).

by resolved waves (Andrews et al. 1987; Sigmond and Scinocca 2010; Sandu et al. 2016; Xu et al. 2019; Eichinger et al. 2020; Šácha et al. 2021), through a process called catalytic wave–mean-flow positive feedback by White et al. (2021). That is, stratospheric OGWD can decelerate the zonal winds, which is conductive to upward propagation of Rossby waves. Then the convergence of the Eliassen–Palm (EP) flux associated with these Rossby waves can further decelerate the polar stratospheric winds.

To investigate the impacts of resolved waves on the stratospheric zonal winds, the zonal-mean EP flux in the Northern Hemisphere is calculated for two experiments following Edmon et al. (1980). Figure 8a displays the zonal-mean EP flux arrows in EXP_KD05. Resolved waves originate from the lower troposphere of midlatitudes and propagate upward, separating into two branches in the upper troposphere. The first branch turns to propagate equatorward across the tropospheric jet, while the other one continues to propagate upward into the stratosphere. Of particular interest is the latter branch, which directly affects the polar stratospheric winds. Figure 8b illustrates the differences between the zonal-mean EP fluxes in these two experiments (i.e., EXP_X21 minus EXP_KD05). The resolved waves in the mid- to lower troposphere below about 400 hPa are enhanced in EXP_X21. Yet, their upward propagation into the upper troposphere and lower stratosphere is suppressed, leading to a net divergence of EP flux which corresponds to positive resolved wave forcing. This is opposed to the well-known compensation mechanism (Cohen et al. 2013), which is caused by the modification of the propagation conditions of resolved waves (Eichinger et al. 2020; Šácha et al. 2021; Hájková and Šácha 2024). The stronger stratospheric winds (as a result of weakened OGWD) narrow the range of wavenumbers that can propagate into the stratosphere (Charney and Drazin 1961).

The vertical propagation of planetary waves can be quantified by the refractive index (RFI) (e.g., Chen and Robinson 1992; Hu et al. 2019):

$$\mathrm{RFI} = \left[\frac{\overline{q_\varphi}}{a\overline{u}} - \left(\frac{k}{a\cos\varphi}\right)^2 - \left(\frac{f}{2NH}\right)^2\right]a^2, \tag{13}$$

where a, k, u, f, N, H, φ, and Ω are Earth's radius, zonal wavenumber, zonal wind, Coriolis parameter, buoyancy frequency, density scale height, latitude, and Earth's angular frequency, respectively; and $\overline{q_\varphi}$ is the meridional gradient of potential vorticity given by

$$\overline{q_\varphi} = 2\Omega\cos\varphi - \left[\frac{(\overline{u}\cos\varphi)_\varphi}{a\cos\varphi}\right]_\varphi + \frac{af^2}{R_d}\left(\frac{p\theta}{T}\frac{\overline{u}_p}{\overline{\theta}_p}\right)_p, \tag{14}$$

with p, θ, T, and R_d being the pressure, potential temperature, temperature and gas constant for dry air, respectively. The subscripts φ and p denote derivatives with respect to latitude and pressure, respectively, while the overbar denotes time and zonal average.

Figure 9a shows the distribution of the RFI for wavenumber 1 resolved waves in experiment EXP_KD05. Positive RFIs are found in the mid- to high latitudes of the Northern Hemisphere, which are supportive of vertical propagation of wavenumber-1 resolved waves. Figure 9b presents the difference between the refractive index of wavenumber 1 resolved waves in the two experiments of EXP_KD05 and EXP_X21. Clearly, in the mid- to high latitudes of the Northern Hemisphere where the zonal-mean zonal winds are enhanced (Fig. 8b), the RFI is decreased, which is not as conducive to the upward propagation of wavenumber 1 resolved waves. Similar results can be found for wavenumber-2 resolved waves (Figs. 9c,d). Higher-wavenumber waves are in general trapped in the troposphere (figure not shown). Therefore, in addition to the weakened OGWD in

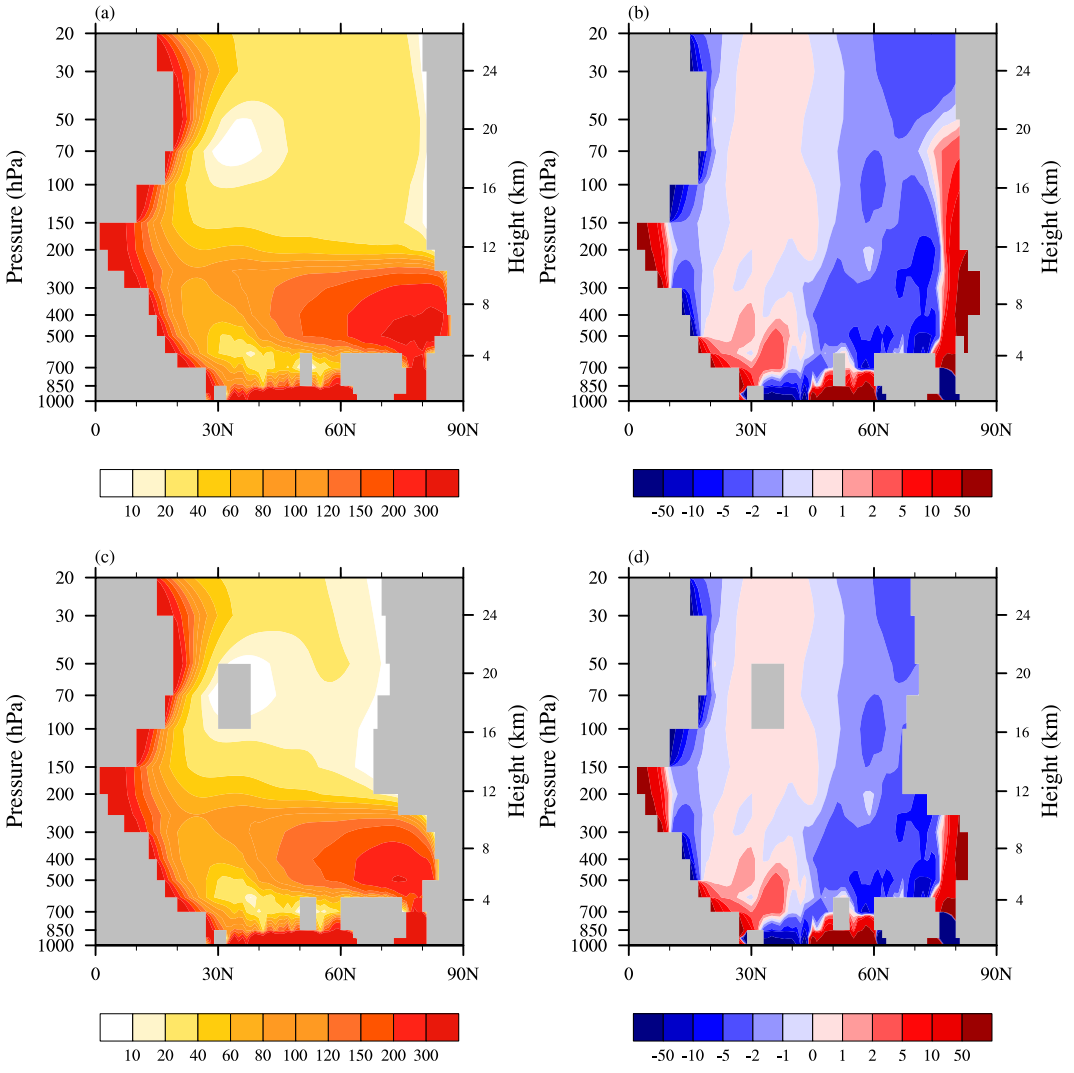

FIG. 9. Refractive index for the (a) wavenumber-1 and (c) wavenumber-2 resolved waves averaged over December 1980–2014 in the EXP_KD05 experiment. Negative values are shaded in gray. (b) The difference between the refractive indices of wavenumber 1 in EXP_X21 and EXP_KD05 (EXP_X21 minus EXP_KD05). (d) As in (b), but for wavenumber 2.

the stratosphere, the suppressed upward propagation of low-frequency resolved waves into the stratosphere also helps reduce the easterly wind biases in the Northern Hemisphere's polar stratosphere. In addition, in the lower troposphere of 45°–60°N, the RFI is increased for both wavenumbers 1 and 2 (Figs. 9b,d), which may explain the enhanced upward propagation of resolved waves there (Fig. 8b).

The changes of the zonal-mean zonal winds in the Southern Hemisphere are much weaker than their Northern Hemisphere counterparts. The largest differences also occur in the high latitudes where NHE are evident (Fig. 2). But the zonal winds are only slightly reduced (<1 m s^{-1}) which does not pass the significance test at the 95% confidence level. This may be due to the fact that the enhancement of stratospheric OGWD near 70°S is weaker than the weakening of OGWD in the Northern Hemisphere's polar stratosphere. The stratospheric OGWD is even reduced to the south of 80°S, i.e., contrary to what happens near 70°S. Furthermore, in December (i.e., austral summer), the polar stratosphere of the Southern Hemisphere is dominated by easterlies (Fig. 7a), which act to inhibit the upward propagation of Rossby waves into the stratosphere (figure showing the corresponding EP flux omitted here). Thus, changes of stratospheric OGWD cannot in that case effectively initiate the catalytic wave–mean-flow positive feedback similar to that found in the polar stratosphere of the Northern Hemisphere.

4. Summary and discussion

In accordance with the asymptotic solution for the surface wave momentum flux (WMF) of nonhydrostatic orographic gravity waves (OGWs) derived in X21, the parameterization

scheme of orographic gravity wave drag (OGWD) developed by Kim and Doyle (2005, KD05) is modified here to account for nonhydrostatic effects (NHE). The revised scheme is then implemented in the MPAS model to investigate NHE on the vertical momentum transport by OGWs and its impact on the atmospheric general circulation during boreal winter. Two sets of global simulations with 30-km resolution are conducted using the original KD05 scheme and the revised one for the December months of 1980–2014.

Results show that the NHE corrections to the surface WMF are most important over regions of complex terrain such as the Tibetan Plateau, Rocky Mountains, southern Andes, and eastern Antarctica where the subgrid-scale orography (SSO) is relatively narrow. Compared with the original KD05 scheme, the revised scheme primarily decreases the surface WMF of parameterized OGWs in the midlatitudes of the Northern Hemisphere. The weakened WMF implies a reduction of wave amplitude which can suppress gravity wave breaking in the lower troposphere. As a result, more WMF is transported upward to higher levels which consequently enhances the OGWD in the upper troposphere and lower stratosphere. On the contrary, enhancement of lower-tropospheric WMF is found near 50° and 70°S as well as north of about 60°N. This is because, despite the fact that NHE decrease the surface WMF relative to hydrostatic linear wave theory, the interaction/feedback between the parameterized model physics and resolved dynamics dominates locally. The revision to the OGWD scheme significantly reduces the easterly wind biases in the polar stratosphere of the Northern Hemisphere where the stratospheric OGWD is weakened. EP flux and refractive index analyses reveal that the upward propagation of resolved waves into the polar stratosphere is suppressed with the revised scheme, leading to a decrease of resolved wave forcing, which also contributes to the reduction of easterly wind biases. In contrast, the revised scheme has a weak impact on the zonal-mean zonal winds in the Southern Hemisphere during boreal winter.

To sum up, this work develops a physically based nonhydrostatic OGWD scheme using simple enough analytical formulas to more accurately represent the momentum transport of OGWs. Preliminary tests in the MPAS model show that the revised OGWD scheme can help improve the simulation of polar stratospheric circulation in the Northern Hemisphere in winter. However, the introduction of NHE to the OGWD parameterization brings only modest changes to the 30-km resolution global simulation, which suggests that such changes may not be a priority for the improvement of OGWD parameterizations in coarse-resolution climate models. Current OGWD parameterizations still have many other shortcomings which deserve more detailed study, e.g., they assume exclusively vertical and instantaneous wave propagation (i.e., flow stationarity) (Ribstein and Achatz 2016; Kalisch et al. 2014; Xu et al. 2017a). It should also be noted that the present work only accounts for NHE on vertically propagating OGWs. The effect of, for example, trapped lee waves (which are intrinsically nonhydrostatic) on the flow near the surface has not been considered. Moreover, the wave breaking criterion in the revised OGWD scheme used here still assumes a hydrostatic dispersion relation. A theory on nonhydrostatic OGW breaking requires further study. The approach adopted here, despite its relatively modest impacts on the results, can be seen as physically accurate, effective and computationally cheap way to include a scale aware (and flow dependent) gradual decay due to NHE of the OGWD associated with the shortest OGWs. It replaces, with clear advantage for that purpose, the abrupt cutoff at an arbitrarily defined scale implemented in many parameterization schemes.

Acknowledgments. This work is mainly supported by the National Science Foundation of China (42122036), the Second Tibetan Plateau Scientific Expedition and Research (STEP) program (2019QZKK0105), the National Science Foundation of China (91837207, 42230607), and the CMA numerical model development project (CXFZ2022M001). The authors are very grateful to the anonymous reviewers for their constructive comments and suggestions.

Data availability statement. The ERA-I data can be freely downloaded from https://www.ecmwf.int/en/forecasts/datasets/reanalysis-datasets/era-interim/. The MPAS model outputs are uploaded to https://doi.org/10.6084/m9.figshare.22082039.

REFERENCES

Alexander, M. J., and Coauthors, 2010: Recent developments in gravity-wave effects in climate models and the global distribution of gravity-wave momentum flux from observations and models. *Quart. J. Roy. Meteor. Soc.*, **136**, 1103–1124, https://doi.org/10.1002/qj.637.

Andrews, D. G., J. R. Holton, and C. B. Leovy, 1987: *Middle Atmosphere Dynamics*. Academic Press, 489 pp.

Charney, J. G., and P. G. Drazin, 1961: Propagation of planetary-scale disturbances from the lower into the upper atmosphere. *J. Geophys. Res.*, **66**, 83–109, https://doi.org/10.1029/JZ066i001p00083.

Chen, P., and W. A. Robinson, 1992: Propagation of planetary waves between the troposphere and stratosphere. *J. Atmos. Sci.*, **49**, 2533–2545, https://doi.org/10.1175/1520-0469(1992)049<2533:POPWBT>2.0.CO;2.

Choi, H.-J., and S.-Y. Hong, 2015: An updated subgrid orographic parameterization for global atmospheric forecast models. *J. Geophys. Res. Atmos.*, **120**, 12 445–12 457, https://doi.org/10.1002/2015JD024230.

——, S.-J. Choi, M.-S. Koo, J.-E. Kim, Y. C. Kwon, and S.-Y. Hong, 2017: Effects of parameterized orographic drag on weather forecasting and simulated climatology over East Asia during boreal summer. *J. Geophys. Res. Atmos.*, **122**, 10 669–10 678, https://doi.org/10.1002/2017JD026696.

Cohen, N. Y., E. P. Gerber, and O. Bühler, 2013: Compensation between resolved and unresolved wave driving in the stratosphere: Implications for downward control. *J. Atmos. Sci.*, **70**, 3780–3798, https://doi.org/10.1175/JAS-D-12-0346.1.

Dee, D. P., and Coauthors, 2011: The ERA-interim reanalysis: Configuration and performance of the data assimilation system. *Quart. J. Roy. Meteor. Soc.*, **137**, 553–597, https://doi.org/10.1002/qj.828.

de la Cámara, A., F. Lott, V. Jewtoukoff, R. Plougonven, and A. Hertzog, 2016: On the gravity wave forcing during the southern stratospheric final warming in LMDZ. *J. Atmos. Sci.*, **73**, 3213–3226, https://doi.org/10.1175/JAS-D-15-0377.1.

Edmon, H. J., Jr., B. J. Hoskins, and M. E. McIntyre, 1980: Eliassen-Palm cross sections for the troposphere. *J. Atmos. Sci.*, **37**, 2600–2616, https://doi.org/10.1175/1520-0469(1980)037<2600:EPCSFT>2.0.CO;2.

Ehard, B., and Coauthors, 2017: Horizontal propagation of large-amplitude mountain waves in the vicinity of the polar night jet. *J. Geophys. Res. Atmos.*, **122**, 1423–1436, https://doi.org/10.1002/2016JD025621.

Eichinger, R., H. Garny, P. Šácha, J. Danker, S. Dietmüller, and S. Oberländer-Hayn, 2020: Effects of missing gravity waves on stratospheric dynamics; Part 1: Climatology. *Climate Dyn.*, **54**, 3165–3183, https://doi.org/10.1007/s00382-020-05166-w.

Fritts, D. C., and M. J. Alexander, 2003: Gravity wave dynamics and effects in the middle atmosphere. *Rev. Geophys.*, **41**, 1003, https://doi.org/10.1029/2001RG000106.

Garcia, R. R., A. K. Smith, D. E. Kinnison, A. de la Cámara, and D. J. Murphy, 2017: Modification of the gravity wave parameterization in the Whole Atmosphere Community Climate Model: Motivation and results. *J. Atmos. Sci.*, **74**, 275–291, https://doi.org/10.1175/JAS-D-16-0104.1.

Hájková, D., and P. Šácha, 2024: Parameterized orographic gravity wave drag and dynamical effects in CMIP6 models. *Climate Dyn.*, **62**, 2259–2284, https://doi.org/10.1007/s00382-023-07021-0.

Hasha, A., O. Bühler, and J. Scinocca, 2008: Gravity wave refraction by three-dimensionally varying winds and the global transport of angular momentum. *J. Atmos. Sci.*, **65**, 2892–2906, https://doi.org/10.1175/2007JAS2561.1.

Hu, D., Y. Guo, and Z. Guan, 2019: Recent weakening in the stratospheric planetary wave intensity in early winter. *Geophys. Res. Lett.*, **46**, 3953–3962, https://doi.org/10.1029/2019GL082113.

Jiang, Q., A. Reinecke, and J. D. Doyle, 2014: Orographic wave drag over the Southern Ocean: A linear theory perspective. *J. Atmos. Sci.*, **71**, 4235–4252, https://doi.org/10.1175/JAS-D-14-0035.1.

Kalisch, S., P. Preusse, M. Ern, S. D. Eckerman, and M. Riese, 2014: Differences in gravity wave drag between realistic oblique and assumed vertical propagation. *J. Geophys. Res. Atmos.*, **119**, 10 081–10 099, https://doi.org/10.1002/2014JD021779.

Kim, Y.-J., and A. Arakawa, 1995: Improvement of orographic gravity wave parameterization using a mesoscale gravity wave model. *J. Atmos. Sci.*, **52**, 1875–1902, https://doi.org/10.1175/1520-0469(1995)052<1875:IOOGWP>2.0.CO;2.

——, and J. D. Doyle, 2005: Extension of an orographic-drag parameterization scheme to incorporate orographic anisotropy and flow blocking. *Quart. J. Roy. Meteor. Soc.*, **131**, 1893–1921, https://doi.org/10.1256/qj.04.160.

Klemp, J. B., and D. R. Durran, 1983: An upper boundary condition permitting internal gravity wave radiation in numerical mesoscale models. *Mon. Wea. Rev.*, **111**, 430–444, https://doi.org/10.1175/1520-0493(1983)111<0430:AUBCPI>2.0.CO;2.

Kruse, C. G., R. B. Smith, and S. D. Eckermann, 2016: The midlatitude lower-stratospheric mountain wave "valve layer." *J. Atmos. Sci.*, **73**, 5081–5100, https://doi.org/10.1175/JAS-D-16-0173.1.

——, and Coauthors, 2022: Observed and modeled mountain waves from the surface to the mesosphere near the Drake Passage. *J. Atmos. Sci.*, **79**, 909–932, https://doi.org/10.1175/JAS-D-21-0252.1.

Li, R., X. Xu, X. Xu, T. G. Shepherd, and Y. Wang, 2023: Importance of orographic gravity waves over the Tibetan Plateau on the spring rainfall in East Asia. *Sci. China Earth Sci.*, **66**, 2594–2602, https://doi.org/10.1007/s11430-023-1204-6.

Lindzen, R. S., 1981: Turbulence and stress owing to gravity wave and tidal breakdown. *J. Geophys. Res.*, **86**, 9707–9714, https://doi.org/10.1029/JC086iC10p09707.

Lott, F., and M. J. Miller, 1997: A new sub-grid orographic drag parameterization: Its formulation and testing. *Quart. J. Roy. Meteor. Soc.*, **123**, 101–127, https://doi.org/10.1002/2014JD021779.

Lu, Y., T. Wu, X. Xu, L. Zhang, and M. Chu, 2020: Improved simulation of the Antarctic stratospheric final warming by modifying the orographic gravity wave parameterization in the Beijing climate center atmospheric general circulation model. *Atmosphere*, **11**, 576, https://doi.org/10.3390/atmos11060576.

McFarlane, N. A., 1987: The effect of orographically excited gravity wave drag on the general circulation of the lower stratosphere and troposphere. *J. Atmos. Sci.*, **44**, 1775–1800, https://doi.org/10.1175/1520-0469(1987)044<1775:TEOOEG>2.0.CO;2.

McLandress, C., T. G. Shepherd, S. Polavaparu, and S. R. Beagley, 2012: Is missing orographic gravity wave drag near 60°S the cause of the stratospheric zonal wind biases in chemistry–climate models? *J. Atmos. Sci.*, **69**, 802–818, https://doi.org/10.1175/JAS-D-11-0159.1.

Miranda, P. M. A., and I. N. James, 1992: Non-linear three-dimensional effects on gravity-wave drag: Splitting flow and breaking waves. *Quart. J. Roy. Meteor. Soc.*, **118**, 1057–1081, https://doi.org/10.1002/qj.49711850803.

Palmer, T. N., G. J. Shutts, and R. Swinbank, 1986: Alleviation of systematic westerly bias in general circulation and numerical weather prediction models through an orographic gravity wave drag parameterization. *Quart. J. Roy. Meteor. Soc.*, **112**, 1001–1039, https://doi.org/10.1002/qj.49711247406.

Polichtchouk, I., A. van Niekerk, and N. Wedi, 2023: Resolved gravity waves in the extra-tropical stratosphere: Effect of horizontal resolution increase from O(10 km) to O(1 km). *J. Atmos. Sci.*, **80**, 473–486, https://doi.org/10.1175/JAS-D-22-0138.1.

Ribstein, B., and U. Achatz, 2016: The interaction between gravity waves and solar tides in a linear tidal model with a 4-D ray-tracing gravity-wave parameterization. *J. Geophys. Res. Space Phys.*, **121**, 8936–8950, https://doi.org/10.1002/2016JA022478.

Šácha, P., A. Kuchar, R. Eichinger, P. Pisoft, C. Jacobi, and H. E. Rieder, 2021: Diverse dynamical response to orographic gravity wave drag hotspots—A zonal mean perspective. *Geophys. Res. Lett.*, **48**, e2021GL093305, https://doi.org/10.1029/2021GL093305.

Sandu, I., P. Bechtold, A. Beljaars, A. Bozzo, F. Pithan, T. G. Shepherd, and A. Zadra, 2016: Impacts of parameterized orographic drag on the Northern Hemisphere winter circulation. *J. Adv. Model. Earth Syst.*, **8**, 196–211, https://doi.org/10.1002/2015MS000564.

——, and Coauthors, 2019: Impacts of orography on large-scale atmospheric circulation. *npj Climate Atmos. Sci.*, **2**, 10, https://doi.org/10.1038/s41612-019-0065-9.

Sato, K., S. Tateno, S. Watanabe, and Y. Kawatani, 2012: Gravity wave characteristics in the Southern Hemisphere revealed by a high-resolution middle-atmosphere general circulation model. *J. Atmos. Sci.*, **69**, 1378–1396, https://doi.org/10.1175/JAS-D-11-0101.1.

Scinocca, J. F., and N. A. McFarlane, 2000: The parametrization of drag induced by stratified flow over anisotropic orography. *Quart. J. Roy. Meteor. Soc.*, **126**, 2353–2393, https://doi.org/10.1002/qj.49712656802.

Shepherd, T. G., 2014: Atmospheric circulation as a source of uncertainty in climate change projections. *Nat. Geosci.*, **7**, 703–708, https://doi.org/10.1038/ngeo2253.

Shutts, G., 1995: Gravity-wave drag parameterization over complex terrain: The effect of critical-level absorption in directional wind-shear. *Quart. J. Roy. Meteor. Soc.*, **121**, 1005–1021, https://doi.org/10.1002/qj.49712152504.

Sigmond, M., and J. F. Scinocca, 2010: The influence of the basic state on the Northern Hemisphere circulation response to climate change. *J. Climate*, **23**, 1434–1446, https://doi.org/10.1175/2009JCLI3167.1.

Skamarock, W. C., and Coauthors, 2008: A description of the Advanced Research WRF version 3. NCAR Tech. Note NCAR/TN-475+STR, 113 pp., https://doi.org/10.5065/D68S4MVH.

——, J. B. Klemp, M. G. Duda, L. D. Fowler, S.-H. Park, and T. D. Ringler, 2012: A multiscale nonhydrostatic atmospheric model using centroidal Voronoi tesselations and C-grid staggering. *Mon. Wea. Rev.*, **140**, 3090–3105, https://doi.org/10.1175/MWR-D-11-00215.1.

Song, I.-S., and H.-Y. Chun, 2008: A Lagrangian spectral parameterization of gravity wave drag induced by cumulus convection. *J. Atmos. Sci.*, **65**, 1204–1224, https://doi.org/10.1175/2007JAS2369.1.

Teixeira, M. A. C., P. M. A. Miranda, and R. M. Cardoso, 2008: Asymptotic gravity wave drag expression for non-hydrostatic rotating flow over a ridge. *Quart. J. Roy. Meteor. Soc.*, **134**, 271–276, https://doi.org/10.1002/qj.196.

van Niekerk, A., and Coauthors, 2020: COnstraining ORographic Drag Effects (COORDE): A model comparison of resolved and parametrized orographic drag. *J. Adv. Model. Earth Sys.*, **12**, e2020MS002160, https://doi.org/10.1029/2020MS002160.

——, S. B. Vosper, and M. A. C. Teixeira, 2023: Accounting for the three-dimensional nature of mountain waves: Parametrizing partial critical level filtering. *Quart. J. Roy. Meteor. Soc.*, **149**, 515–536, https://doi.org/10.1002/qj.4421.

Webster, S., A. R. Brown, D. R. Cameron, and C. P. Jones, 2003: Improvements to the representation of orography in the Met Office unified model. *Quart. J. Roy. Meteor. Soc.*, **129**, 1989–2010, https://doi.org/10.1256/qj.02.133.

White, R. H., J. M. Wallace, and D. S. Battisti, 2021: Revisiting the role of mountains in the Northern Hemisphere winter atmospheric circulation. *J. Atmos. Sci.*, **78**, 2221–2235, https://doi.org/10.1175/JAS-D-20-0300.1.

Xu, X., J. Song, Y. Wang, and M. Xue, 2017a: Quantifying the effect of horizontal propagation of three-dimensional mountain waves on the wave momentum flux using Gaussian beam approximation. *J. Atmos. Sci.*, **74**, 1783–1798, https://doi.org/10.1175/JAS-D-16-0275.1.

——, Y. Wang, M. Xue, and K. Zhu, 2017b: Impacts of horizontal propagation of orographic gravity waves on the wave drag in the stratosphere and lower mesosphere. *J. Geophys. Res. Atmos.*, **122**, 11 301–11 312, https://doi.org/10.1002/2017JD027528.

——, Y. Tang, Y. Wang, and M. Xue, 2018: Directional absorption of mountain waves and its influence on the wave momentum transport in the Northern Hemisphere. *J. Geophys. Res. Atmos.*, **123**, 2640–2654, https://doi.org/10.1002/2017JD027968.

——, M. Xue, M. A. C. Teixeira, J. Tang, and Y. Wang, 2019: Parameterization of directional absorption of orographic gravity waves and its impact on the atmospheric general circulation simulated by the Weather Research and Forecasting Model. *J. Atmos. Sci.*, **76**, 3435–3453, https://doi.org/10.1175/JAS-D-18-0365.1.

——, M. A. C. Teixeira, M. Xue, Y. Lu, and J. Tang, 2020: Impacts of wind profile shear and curvature on the parameterized orographic gravity wave stress in the weather research and forecasting model. *Quart. J. Roy. Meteor. Soc.*, **146**, 3086–3100, https://doi.org/10.1002/qj.3828.

——, R. Li, M. A. C. Teixeira, and Y. Lu, 2021: On the momentum flux of vertically-propagating orographic gravity waves excited in nonhydrostatic flow over three-dimensional orography. *J. Atmos. Sci.*, **78**, 1807–1822, https://doi.org/10.1175/JAS-D-20-0370.1.

Xue, M., and A. J. Thorpe, 1991: A mesoscale numerical model using the nonhydrostatic pressure-based sigma-coordinate equations: Model experiments with dry mountain flows. *Mon. Wea. Rev.*, **119**, 1168–1185, https://doi.org/10.1175/1520-0493(1991)119<1168:AMNMUT>2.0.CO;2.

Zängl, G., 2003: Orographic gravity waves close to the nonhydrostatic limit of vertical propagation. *J. Atmos. Sci.*, **60**, 2045–2063, https://doi.org/10.1175/1520-0469(2003)060<2045:OGWCTT>2.0.CO;2.

Zhang, R., X. Xu, and Y. Wang, 2020: Impacts of subgrid orographic drag on the summer monsoon circulation and precipitation in East Asia. *J. Geophys. Res. Atmos.*, **125**, e2019JD032337, https://doi.org/10.1029/2019JD032337.

Zhou, X., A. Beljaars, Y. Wang, B. Huang, C. Lin, Y. Chen, and H. Wu, 2017: Evaluation of WRF simulations with different selections of subgrid orographic drag over the Tibetan Plateau. *J. Geophys. Res. Atmos.*, **122**, 9759–9772, https://doi.org/10.1002/2017JD027212.